

Research Article

Mechanical Properties and Numerical Analyses of Basalt Fiber Crumb Rubber Mortars in Soft Rock Roadways

Jun-Ling Qin , Wei-Guo Qiao , Deng-Ge Lin, Shuai Zhang , and Ji-Yao Wang

Shandong Provincial Key Laboratory of Civil Engineering Disaster Prevention and Mitigation,
College of Civil Engineering and Architecture, Shandong University of Science and Technology, Qingdao 266590, China

Correspondence should be addressed to Wei-Guo Qiao; qiaowg1@163.com

Received 1 May 2019; Revised 21 June 2019; Accepted 18 July 2019; Published 14 August 2019

Academic Editor: Wayne Yu Wang

Copyright © 2019 Jun-Ling Qin et al. This is an open access article distributed under the Creative Commons Attribution License, which permits unrestricted use, distribution, and reproduction in any medium, provided the original work is properly cited.

The strength of crumb rubber mortars can be improved by the addition of basalt fibers. However, limited studies have been conducted on basalt fiber crumb rubber mortars (BF-CRM), and the constitutive model is still very immature. In this paper, uniaxial compressive stress-strain curves are obtained for several groups of BF-CRM specimens with different contents. By comparison with the GZH model, modified GZH parameters that can be used in a BF-CRM constitutive model are obtained. Then, taking the support scheme of the main substation of a mine as the background, FLAC3D is used to simulate the roadway support, BF-CRM replaces the ordinary mortars in the original support, and triaxial compression tests are performed at different confining pressures. In this way, the application of BF-CRM in roadway support is studied and analyzed.

1. Introduction

The addition of crumb rubber to engineering materials, such as cement mortar, not only improves the ductility, durability, and impact resistance of these materials but also promotes the reuse of waste rubber [1–5]. Basalt fiber is a kind of silicate fiber that is processed from volcanic rock ore and offers the advantages of high tensile strength, high temperature resistance, corrosion resistance, and stable chemical properties [6, 7]. Crumb rubber or basalt fibers are incorporated into traditional building materials to form new composite building materials that have been widely introduced into pavement engineering, protection engineering, high-speed railways, and underground space engineering [8, 9].

In recent years, scholars worldwide have conducted many research studies on composite-material-based cement mortars. Yan et al. [10] studied the effect of adding rubber powder to fresh and hardened mortars. The results showed improvements in the workability of fresh mortar and in the deformability, early strength, and frost resistance of hardened mortar. Long et al. [11, 12] studied the mechanical properties of cement concrete containing waste rubber

particles of different sizes. Richardson et al. [13, 14] used rubber crumb as an air-entraining admixture in concrete and carried out freeze-thaw tests, which showed that rubber crumb was effective in providing freeze/thaw protection. Yu and Zhu [2] found that the consistency and initial density of cement mortar decreased as the rubber particle size increased and the porosity of the mortar increased as the rubber particle size decreased. Di et al. [15] found a strong correlation between the damage threshold of CRC (crumb rubber concrete) and the amount of energy that was dissipated at the peak strength, where a CRC containing 25% rubber by mass exhibited the largest damage threshold in laboratory experiments and numerical simulations. Li and Xu [16] studied the effect of adding basalt fibers on the dynamic mechanical properties of concrete under impact loading. It was found that 0.1% basalt fibers was the optimum basalt fiber content for strengthening and toughening concrete. Barabanshchikov and Gutskalov [17] showed that the flexural stability of cement increased with the basalt fiber content and that there was an optimum fiber dose. Fenu et al. [18] conducted static and dynamic tests to study the effects of glass fiber and basalt fiber on the tensile strength, flexural strength, and energy absorption capacity of cement mortar.

The results showed that both fibers increased the energy absorption capacity of cement mortar. Wang et al. [19] studied a CRC that was modified by adding steel fibers and nanosilica. The test results showed that the modified CRC with 1.0% steel fiber content had relatively high compressive and splitting tensile strengths. Santarelli et al. [20] studied the physical and mechanical properties and microstructures of three kinds of hydrated lime mortars with different compositions of basalt fibers. It was found that basalt fibers could delay cracking, improve compressive strength, and reduce the capillary water absorption coefficient of mortar. Song et al. [21] conducted triaxial compression tests under different confining pressures for crumb rubber with various rubber particle contents. According to Lemaitre's strain equivalence principle and the Weibull random distribution, a damage constitutive model for crumb rubber mortars with different rubber particle contents was established.

At present, a series of problems have arisen in the process of deep resource exploitation, among which the failure characteristics of deep high-stress soft rock roadways have become critical such that the effective support of soft rock roadways has attracted the attention of scholars worldwide [22–24]. In this paper, uniaxial and triaxial compression tests were performed on BF-CRM specimens with different contents of basalt fibers and rubber particles. The effects of the basalt fiber and rubber particle content on the compressive strength and compressibility of BF-CRM were studied. The stress-strain curves obtained by these tests were fit using the GZH model [25] to obtain recommended values for BF-CRM constitutive parameters. Then, based on the tunnel support scheme of a mine main substation, using FLAC3D and combined with BF-CRM triaxial compression tests under 5 MPa and 8 MPa confining pressure, the application of BF-CRM in high-stress soft rock roadway support was studied and analyzed.

2. Experimental Study of the Physical Mechanics

2.1. Materials and Mixing Ratio. The chemical composition and physical and mechanical properties of P.O. 42.5 cement produced in Jinan are shown in Table 1. The physical and mechanical properties of short-cut basalt fibers produced by Anji in Zhejiang Province are shown in Table 2. The river sand particles have a maximum size of 5 mm, with a continuous gradation, an apparent density of 2.6 g/cm^3 , a bulk density of 1440 kg/m^3 , a porosity of 45%, and a fineness modulus of 2.4. The rubber particles have a size of 6–8 mm and an apparent density of 1200 g/cm^3 . Before preparing the test specimens, the rubber particles were first immersed in a 10% NaOH solution for 30 minutes. Then, the rubber particles were washed with fresh water until the pH of the solution was 7. The comparison of the particles before and after treatment is shown in Figure 1. The additives mainly consist of water reducers and binders. The water reducer is the superplasticizer DC-WR1 with a water-reducing rate of 18%–25%. The binder used is the DC-W10 polyacrylate emulsion, which was added in the amount of 15% of the total rubber particles.

The mixing ratio of basalt fiber to crumb rubber mortar is shown in Table 3. The water-to-cement ratio is 0.35, and the sand-to-cement ratio is 1.5. The proportion of rubber particles used is 0%, 5%, 10%, 20%, and 30%, which are labeled as A, B, C, D, and E, respectively. Basalt particles are used in the proportions 0%, 0.4%, 0.8%, and 1.2%. For example, the label B-0.4% indicates a rubber particle content of 5% of the total mass of BF-CRM and a basalt fiber content of 0.4% of the total mass of BF-CRM.

2.2. Sample Preparation and Test Methods. Twenty groups of BF-CRM specimens were designed in this experiment. Each group contains four specimens. Three specimens were used for the uniaxial compression test, one was reserved, and the size of the specimens is a $\phi 50 \text{ mm} \times 100 \text{ mm}$ cylinder. A total of 80 specimens were prepared. The specimens were molded and demolded after 24 h and then maintained in a standard environment for 28 days. Then, an MTS rock servo test machine is used for the uniaxial and three-axis compression test. The process of specimen preparation and experimental operation is based on GB/T 50081–2002 for Standard Testing Methods of Mechanical Properties of Ordinary Concrete.

2.3. Results and Discussion. The amount of compression for each group of BF-CRM specimens is determined by averaging the results of 3 tests in each group and is shown in Table 4. Under uniaxial compression, at the same basalt fiber content, the compression of the mortar increases with the rubber particle content. When the rubber particle content is less than 20%, the compression increases more slowly, and when the rubber content is more than 20%, the compression increases more quickly. Increasing the basalt fiber content has a less clear effect than rubber particles on the compression of BF-CRM.

The failure modes of each group of specimens following the uniaxial compression test are shown in Figure 2. For group A specimens without rubber particles, a few small cracks gradually appear in the middle of the specimens during the loading process and spalling phenomena become clearly visible on the specimen surface. After reaching the peak stress, cracks develop toward the upper and lower ends of the specimens, the width increases continuously, and the bearing capacity of the test block decreases rapidly. For groups A–D, the rate of crack growth gradually slows as the basalt fiber content is increased, and the addition of fiber delays the appearance and penetration of cracks. For group E, there are no obvious cracks during loading and the specimens maintain good integrity until the end of loading.

The stress-strain curves of each group are obtained by averaging the results of 3 tests in each group and are shown in Figure 3. By comparing the stress-strain curves with same basalt fiber content, it can be seen that the peak strength of the test block decreases gradually as the rubber particle content increases. For a rubber particle content of 30%, the peak strength of the specimen is only about approximately 1.5 MPa, and the compressive strength is extremely low.

TABLE 1: Physical and mechanical properties of P.O. 42.5 Portland cement.

Density (g/cm^3)	Specific surface area (cm^2/g)	Setting time		Compressive strength (MPa)	Flexural strength (MPa)
		Initial (min)	Final (min)		
3.00 ± 0.02	3450 ± 50	120 ± 5	310 ± 10	48.5 ± 2.0	9.2 ± 0.5

TABLE 2: Physical and mechanical properties of basalt fiber.

Length (mm)	Diameter (μm)	Density (kg/m^3)	Tensile strength (MPa)	Elastic modulus (GPa)	Elongation (%)
20	15	2650	4100–4840	90–110	2.4–3.0

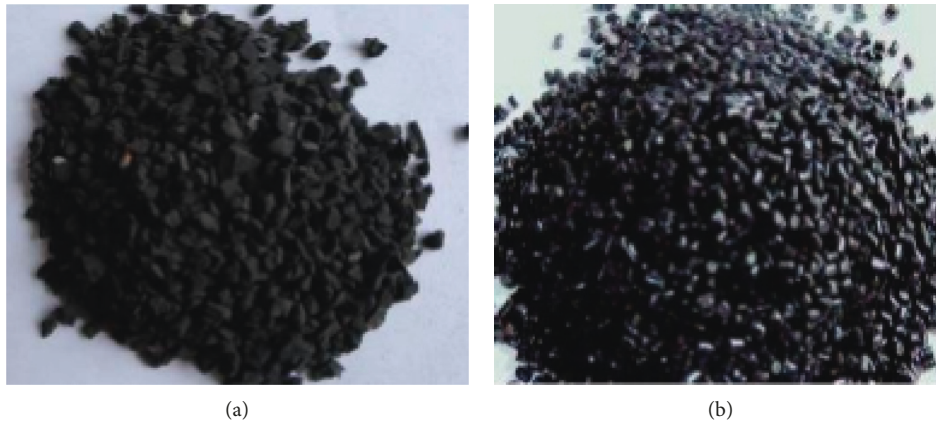


FIGURE 1: Comparison of rubber particles before and after treatment.

TABLE 3: Mixture proportion of basalt fiber rubber mortar (by weight).

Type	Rubber particle	Basalt fiber (%)	Cement	Sand	Water	Water reducer	Binders
A-0%	A	0	1	1.5	0.35	0.015	0
A-0.4%		0.4	1	1.5	0.35	0.015	0
A-0.8%		0.8	1	1.5	0.35	0.015	0
A-1.2%		1.2	1	1.5	0.35	0.015	0
B-0%	B	0	1	1.5	0.35	0.015	0.023
B-0.4%		0.4	1	1.5	0.35	0.015	0.023
B-0.8%		0.8	1	1.5	0.35	0.015	0.023
B-1.2%		1.2	1	1.5	0.35	0.015	0.023
C-0%	C	0	1	1.5	0.35	0.015	0.049
C-0.4%		0.4	1	1.5	0.35	0.015	0.049
C-0.8%		0.8	1	1.5	0.35	0.015	0.049
C-1.2%		1.2	1	1.5	0.35	0.015	0.049
D-0%	D	0	1	1.5	0.35	0.015	0.112
D-0.4%		0.4	1	1.5	0.35	0.015	0.112
D-0.8%		0.8	1	1.5	0.35	0.015	0.112
D-1.2%		1.2	1	1.5	0.35	0.015	0.112
E-0%	E	0	1	1.5	0.35	0.015	0.196
E-0.4%		0.4	1	1.5	0.35	0.015	0.196
E-0.8%		0.8	1	1.5	0.35	0.015	0.196
E-1.2%		1.2	1	1.5	0.35	0.015	0.196

After reaching the peak strength, the ductility of the specimens increases gradually; moreover, as the rubber particle content increases, the compaction stage of the tests increases significantly during the loading process. Increasing the fiber

content shifts the entire experimental stress-strain curve upwards and increases the peak stress. A fiber content of 0.4% corresponds to the maximum increase in the peak stress of the test block.

TABLE 4: Compression of BF-CRM with different proportions.

Type	Compression (mm)
A-0%	0.43
A-0.4%	0.45
A-0.8%	0.47
A-1.2%	0.50
B-0%	0.95
B-0.4%	1.01
B-0.8%	1.10
B-1.2%	1.15
C-0%	1.25
C-0.4%	1.26
C-0.8%	1.28
C-1.2%	1.30
D-0%	1.60
D-0.4%	1.62
D-0.8%	1.64
D-1.2%	1.65
E-0%	3.40
E-0.4%	3.42
E-0.8%	3.45
E-1.2%	3.47



FIGURE 2: Uniaxial failure modes of basalt fiber rubber particles mortar: (a) A group; (b) B group; (c) C group; (d) D group; (e) E group.

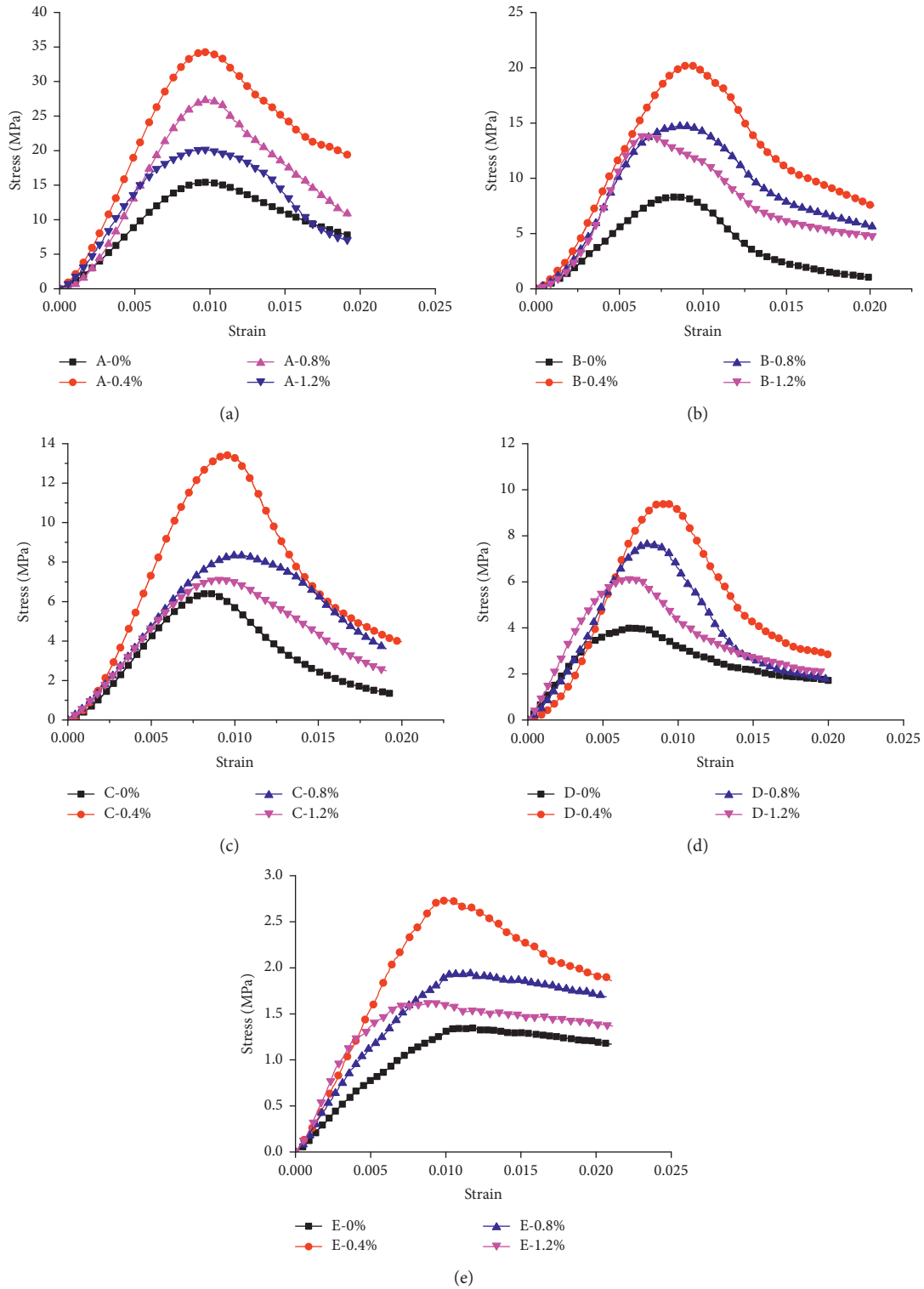


FIGURE 3: Experimental stress-strain curves of BF-CRM under uniaxial compression: (a) A group; (b) B group; (c) C group; (d) D group; (e) E group.

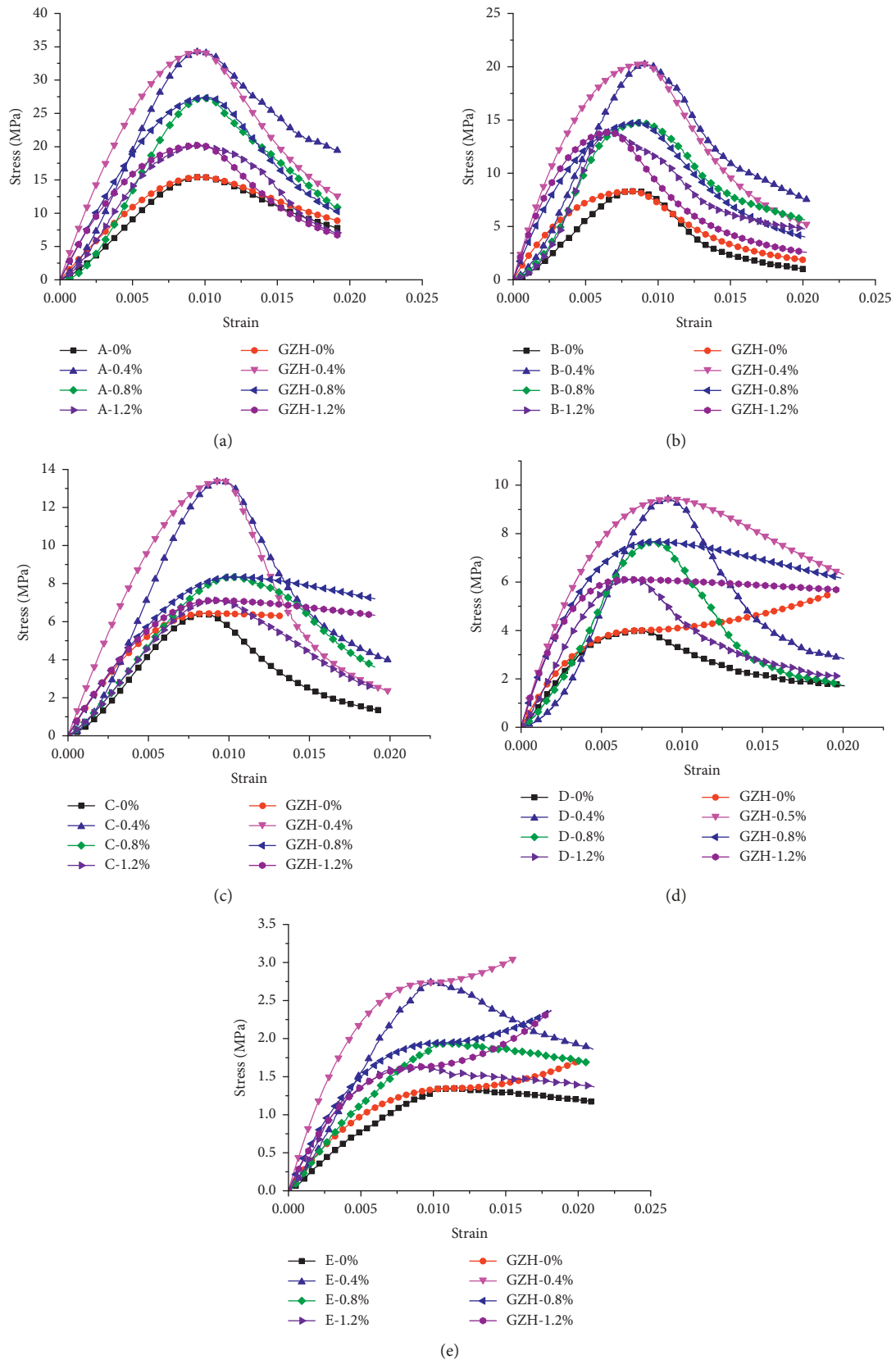


FIGURE 4: Fitting results of the curve of BF-CRM based on the GZH model: (a) A group; (b) B group; (c) C group; (d) D group; (e) E group.

3. Uniaxial Compression Constitutive Model

To analyze the mechanical properties of BF-CRM under uniaxial compression, the experimentally obtained stress-strain curves are evaluated and compared with the GZH model. The results are used to determine improved values for the BF-CRM constitutive parameters.

The GZH model is a piecewise formula for describing the stress-strain curve of ordinary concrete under uniaxial compression that was developed by Guo Zhenhai using experimental test results and is given below:

$$\begin{aligned}
 y &= ax + (3 - 2a)x^2 + (a - 2)x^3, \quad x < 1, \\
 y &= \frac{x}{b(x - 1)^2 + x}, \quad x \leq 1, \\
 x &= \frac{\varepsilon}{\varepsilon_c}, \\
 y &= \frac{\sigma}{f_c},
 \end{aligned} \tag{1}$$

where a and b are the parameters of the constitutive model; σ and ε are the stress and strain, respectively; and f_c and ε_c are the peak stress and peak strain, respectively.

3.1. Comparison of the Stress-Strain Curve with the GZH Model. The experimental stress-strain curves of BF-CRM are compared with the GZH model, as shown in Figure 4. In the rising section of the stress-strain curve, the GZH model is clearly different from the test curve. The GZH model clearly overestimates the bearing capacity of the test groups, except for A-0% and C-0%, and this overestimate depends on the amount of added rubber particles and basalt fiber. In the descending section of the test group curves, especially with increasing rubber particle content, the change of ductility of the test block can be clearly seen. However, the stress calculated using the GZH model is generally lower than the experimentally obtained stress and deviates from the experimentally obtained stress when the experimental peak strength is below 10 MPa. Therefore, it is not appropriate to directly use the GZH model to analyze experimental results for BF-CRM specimens and predict their mechanical behavior.

3.2. Modification of BF-CRM Constitutive Model. At present, the research on BF-CRM is inadequate, and the constitutive model for BF-CRM is relatively immature. Meanwhile, unlike for ordinary cement mortar, the behavior of BF-CRM depends on many factors, such as the rubber particle content, the particle size, and the basalt fiber content. Moreover, a limited number of BF-CRM samples have been studied, so it is not appropriate to present a formula to determine constitutive parameters based on the changes in the particle size, content, and other factors. Therefore, the stress-strain test data are fit to the GZH model to obtain values for the constitutive parameters a and b to obtain a modified GZH model for BF-CRM. These values are shown in Table 5.

The test stress-strain curves are compared with the modified GZH model curve, as shown in Figure 5. The modified GZH model agrees well with the experimental curve, especially in the descending section of the curve, which reflects the ductility of BF-CRM. It is worth noting that the modified GZH model slightly overestimates the material strength in the compression stage of the stress-strain curve.

4. Numerical Simulation of BF-CRM in Roadway Support

In this paper, FLAC3D is used to simulate and analyze a roadway support using the geological conditions and support scheme of a mine main substation channel. The original supporting scheme of the roadway is as follows: after roadway excavation, bolts and U-shaped steel brackets are immediately installed in the surrounding rock and 400 mm ordinary mortar is irrigated above the floor surrounding rock. To explore the effect of using basalt fiber rubber granular mortar in soft rock roadway support engineering applications, the 400 mm ordinary mortar (plan A) in the original roadway support scheme is replaced by 200 mm basalt fiber in rubber granular mortar (plan B).

In the developing the model, the BF-CRM layer is based on the physical and mechanical parameters that are obtained from the B-0.4% group test, and the constitutive relationship was modified. The other model components are constructed according to the field support parameters to better compare and reflect the role of BF-CRM in the support structure.

4.1. Displacement Evolution Characteristics of a Roadway. The vertical displacement of the roadway floor after excavation is shown in Figure 6.

Figure 6(a) shows that plan A is used in the support after 6 m of roadway excavation. The maximum vertical displacement of the floor at $y=0$ m is 437 mm, and the maximum displacement of the floor at $y=5$ m is 400 mm. For the unexplored roadway, the vertical displacement is also changed at $y=10$ m due to the influence of excavation and the maximum change is approximately 12 mm.

Figure 6(b) shows the support in which plan B is used. It can be seen that the maximum vertical displacement of the floor at $y=0$ m, i.e., the location of the floor heave, is only 35 mm; at $y=5$ m, the maximum displacement of the floor is 70 mm; and for the section of the unexplored roadway at $y=10$ m, the vertical displacement also varies with a maximum change of approximately 6 mm under the influence of excavation.

After replacing the ordinary cement mortar with BF-CRM, the floor heave at $y=0$ m is only 1/10th of its value in the original supporting scheme, and the floor heave at $y=6$ m is also significantly reduced. The whole support structure reduces the floor heave deformation.

4.2. Stress Evolution Characteristics of a Roadway. Under the two supporting schemes, the stress changes of surrounding rock after excavation are shown in Figure 7.

TABLE 5: Fitting parameters a and b based on the GZH model.

Type	Fitting parameter a	Fitting parameter b
A-0%	1.007	1.718
A-0.4%	0.641	2.181
A-0.8%	0.158	4.019
A-1.2%	1.447	2.733
B-0%	0.696	5.743
B-0.4%	0.347	2.745
B-0.8%	0.666	2.776
B-1.2%	0.327	1.587
C-0%	0.770	5.530
C-0.4%	0.632	5.129
C-0.8%	1.046	2.852
C-1.2%	1.061	2.651
D-0%	2.350	1.903
D-0.4%	0.132	5.230
D-0.8%	0.654	5.227
D-1.2%	1.424	1.842
E-0%	1.483	0.446
E-0.4%	0.666	1.013
E-0.8%	1.076	0.457
E-1.2%	2.380	0.318

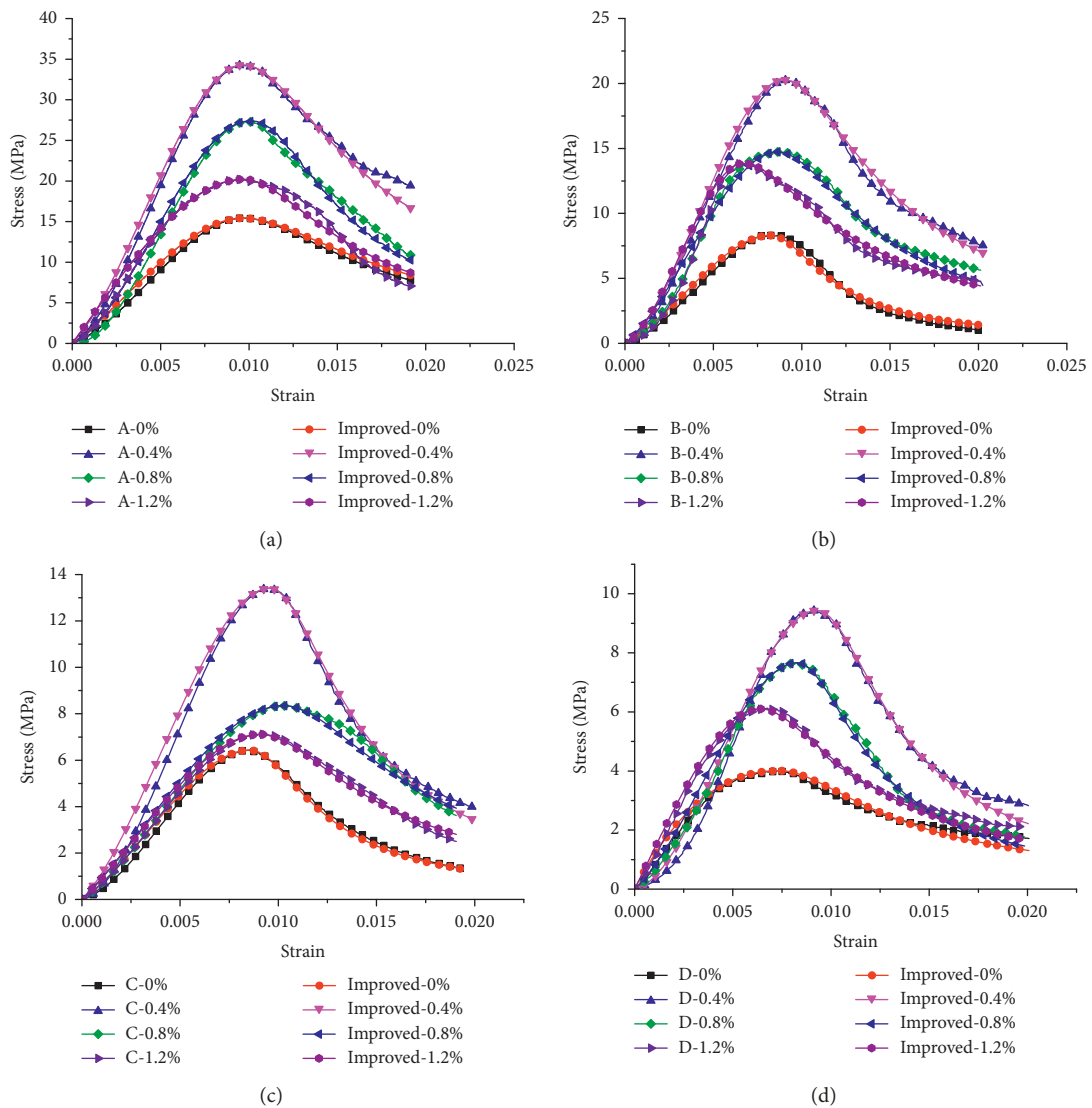


FIGURE 5: Continued.

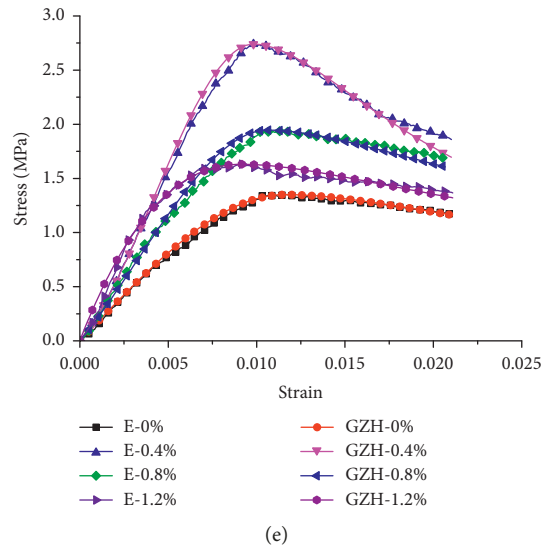


FIGURE 5: Fitting results of the curve of BF-CRM based on the modified GZH model: (a) A group; (b) B group; (c) C group; (d) D group; (e) E group.

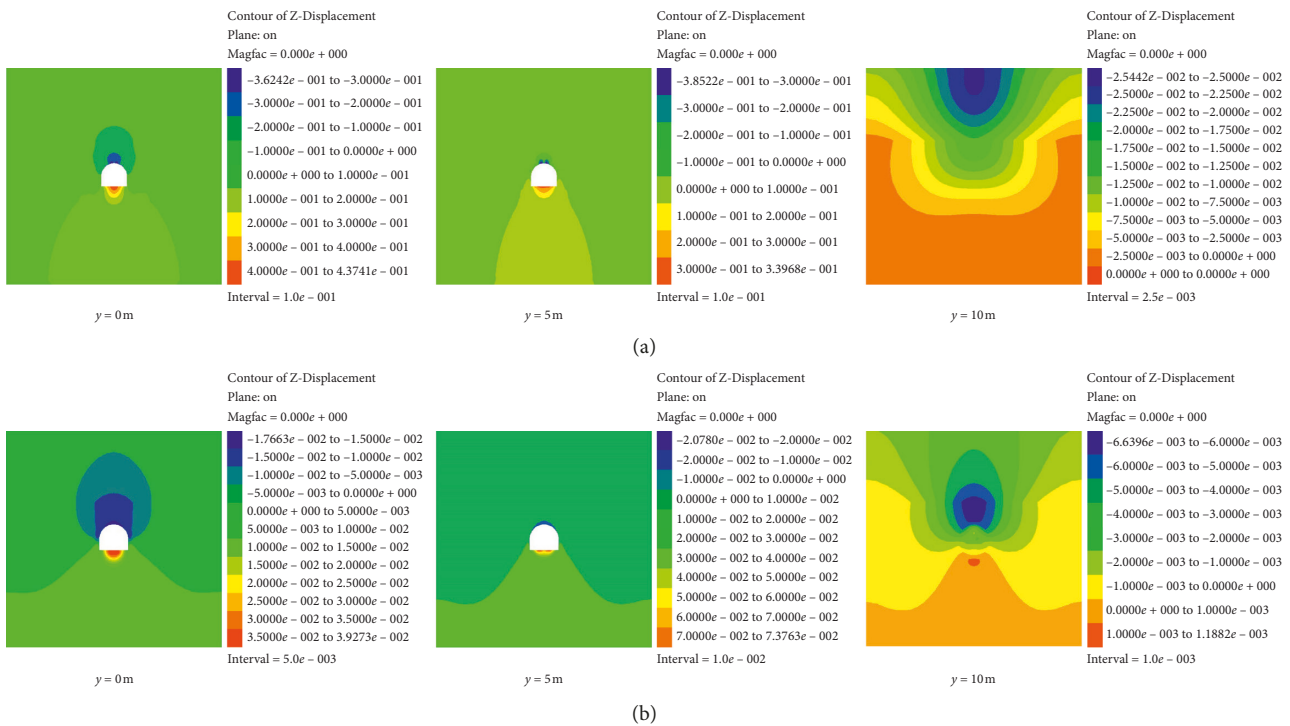


FIGURE 6: Vertical displacement changes of the tunnel floor after excavation: (a) plan A; (b) plan B.

Figure 7(a) shows the use of plan A to support the roadway after a 6 m excavation. At $y=0$ m, the maximum principal stress around the roadway gradually recovers from 2.5 MPa to 22.11 MPa as the distance increases. At $y=5$ m, the maximum principal stress gradually recovers from 2.5 MPa to 22.08 MPa, which is the same as that at $y=0$ m, showing that the maximum principal stress around the

roadway is the same as that over the excavation range. For the section of the untapped roadway, the maximum principal stress at $y=10$ m is also affected and varies similarly to the maximum principal stress at $y=0$ m and $y=5$ m.

Figure 7(b) shows that, using plan B, the maximum principal stress around the roadway gradually recovers from 2.0 MPa to 21.61 MPa at $y=0$ m. At $y=5$ m, the maximum

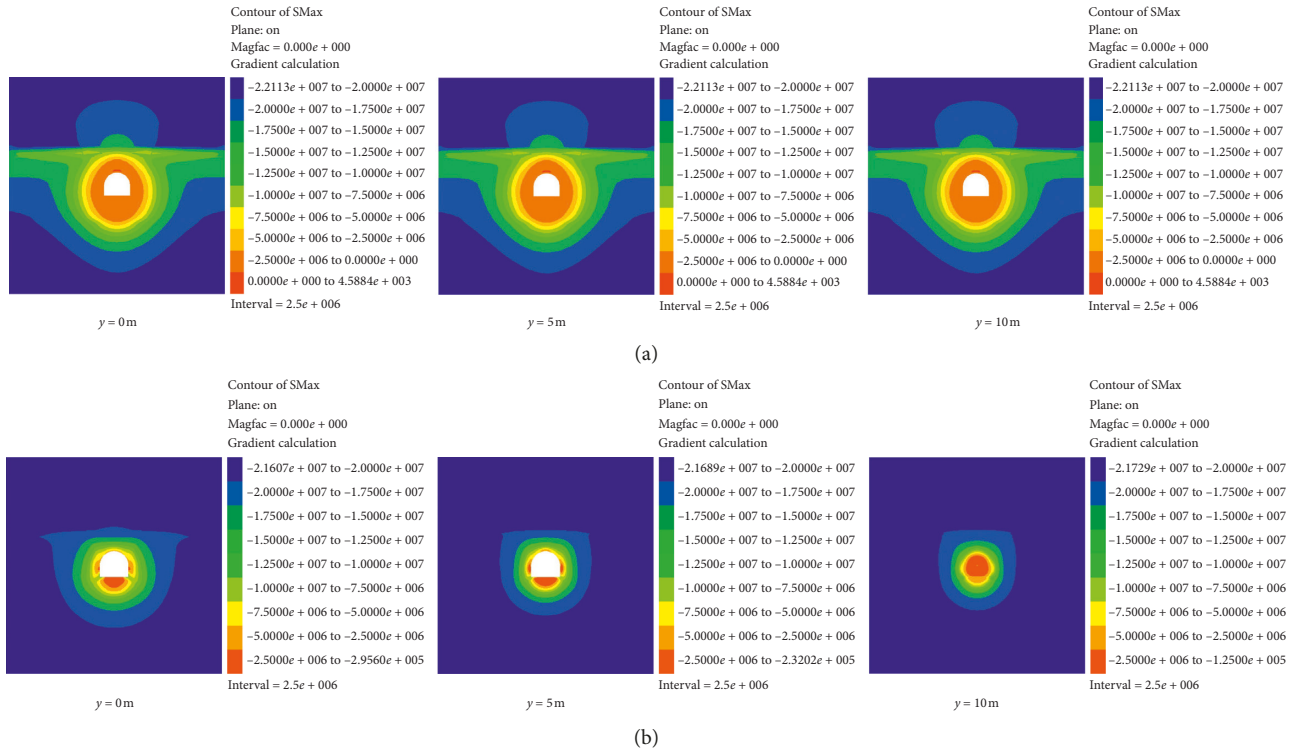


FIGURE 7: Maximum principal stress distribution of the tunnel floor after excavation: (a) plan A; (b) plan B.

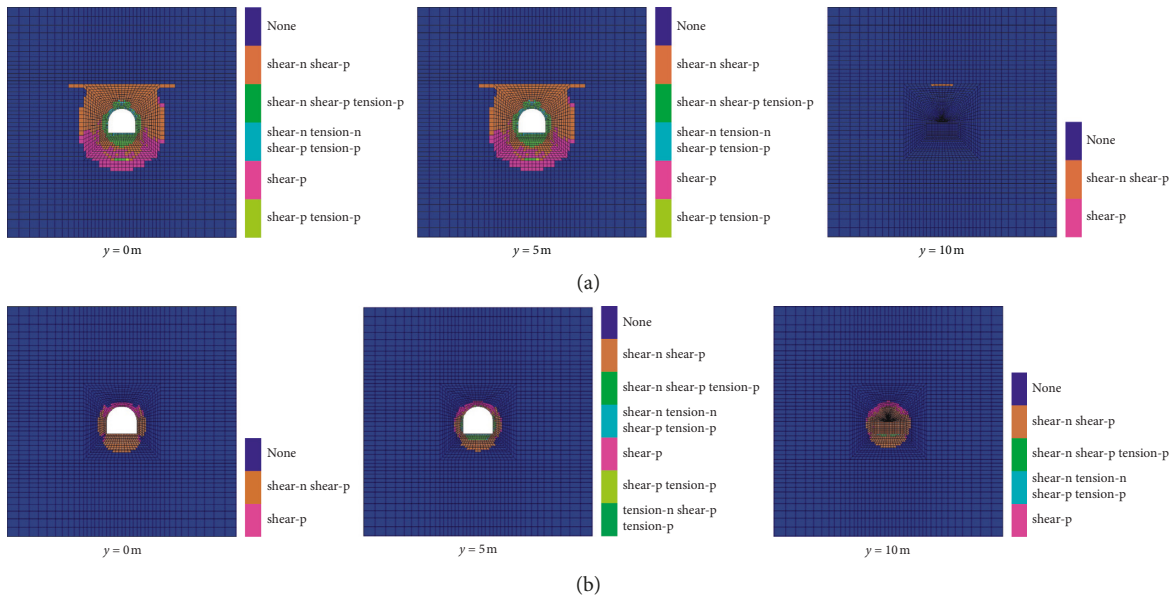


FIGURE 8: Damage mechanism of surrounding rocks of the tunnel floor after excavation: (a) plan A; (b) plan B.

principal stress gradually recovers from 2.0 MPa to 21.61 MPa. The maximum principal stress around the roadway is the same as that over the excavation range. Plans A and B exhibit the same variation in the principal stress, but plan B has a smaller effect on the principal stress. The BF-CRM layer could effectively reduce the influence of excavation on effective stress.

4.3. Damage Characteristics and Surrounding Rock Analysis. The failure characteristics of roadways are mainly determined by analyzing the range over which the plastic zone extends in the surrounding rock during excavation. Figure 8 shows the range over which the plastic zone varies after stress stabilization of the surrounding rock after excavation.

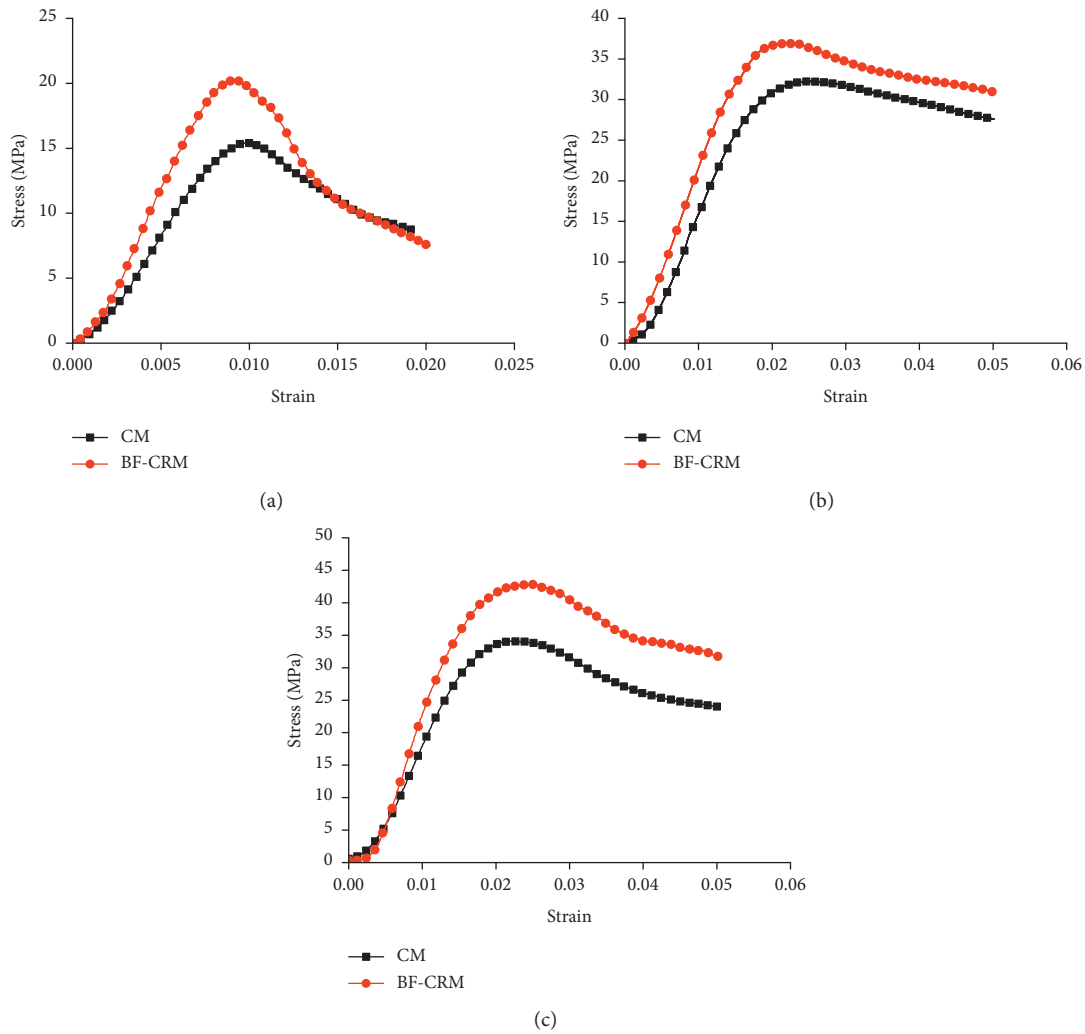


FIGURE 9: Stress-strain curve for the conventional triaxial pressure test: (a) 0 MPa; (b) 5 MPa; (c) 8 MPa.

Figure 8 shows that when plan A is used, the radius of the plastic zone at the floor is approximately 3 m, and the shear stress is the dominant stress in this region. In the middle section of the excavation roadway, the plastic zone is distributed similarly to that in the first excavation section. The difference between the two areas is that the tensile stress in the middle section occurs at $\gamma = 6$ m. The top rock stratum at $\gamma = 10$ m ahead of the excavation is affected by excavation, but there is no complete plastic zone. Figure 8(b) shows the distribution of the plastic zone in the surrounding rock for plan B. The radius of the plastic zone at the floor is approximately 1.5 m, which is only 1/2 of that for plan A. The addition of BF-CRM effectively reduces the range of the plastic zone. However, in the untapped area where $\gamma = 10$ m, there is a small plastic zone that is affected by excavation.

4.4. Mechanism Analysis of the Two Support Schemes. Triaxial compression tests are carried out on common cement mortar (CM) and BF-CRM specimens with B-0.4% under confining pressures of 5 MPa and 8 MPa, respectively, where both types of specimens are made with the same

water-cement ratio. The stress-strain curves for the BF-CRM and CM specimens under different confining pressures are shown in Figure 9.

The entire stress-strain curve for the BF-CRM specimens lies above that of the CM specimens, and the strain energy of BF-CRM is clearly higher than that of CM for the same confining pressure; that is, the same volume of BF-CRM can absorb more deformation energy than CM, and this difference becomes more significant as the confining pressure increases.

Plan B is superior to plan A in controlling the displacement and deformation of the floor, in reducing the stress concentration around the surrounding rock, and in reducing the range of the plastic zone. The main reason for the aforementioned differences is that BF-CRM has a higher compressibility than CM. In the enclosed space between the common CM layer and the surrounding rock, the deformation of the surrounding rock squeezes the BF-CRM layer. However, the large compressibility of BF-CRM enables it to gradually absorb the energy released by the confining pressure deformation, along with the surrounding rock, thus playing the role of an energy

absorbing buffer. Common CM belongs to the class of rigid support materials and has a poor compressibility. Common CM fails even for small deformations of the surrounding rock.

5. Conclusions

- (1) The stress-strain curves of BF-CRM specimens are obtained experimentally. With the increase in rubber particle content, the peak stress for the BF-CRM specimens decreases gradually. The uniaxial compressive strength of BF-CRM can be effectively improved by adding basalt fibers, and its peak strength can be significantly increased by adding 0.4% basalt fibers. Rubber particles can improve the compressibility of cement mortar, whereas basalt fibers have no significant effect on the compressibility of cement mortar, but they can effectively slow the expansion of BF-CRM cracks.
- (2) The experimentally obtained results differ greatly from the predicted values of the GZH model. For stresses below the peak stress, the GZH model overestimates the load-carrying capacity; for stresses greater than the peak stress, the GZH model clearly underestimates the ductility of BF-CRM; and for materials with peak stresses less than 10 MPa, the GZH prediction deviates completely from the experimental stress-strain curve. Thus, the GZH model is not suitable for obtaining a constitutive equation for BF-CRM. The experimental stress-strain curve is fit with the GZH model to obtain revised values for the constitutive parameters of the GZH model. The revised GZH model is in good agreement with the experimental stress-strain curve and can be used as a reference model for the analysis and design of BF-CRM.
- (3) The tunnel support scheme of a mine main substation is considered as the background, and FLAC3D is used to simulate the roadway support. The original support scheme is changed from a 400 mm-sized ordinary CM layer that is poured on the floor to a 200 mm-sized BF-CRM layer that is poured first followed by a 200 mm-sized poured ordinary CM layer. Combined with triaxial compression tests at 5 MPa and 8 MPa confining pressures, the analysis shows that the BF-CRM layer acts as a cushion that absorbs the energy that is released in the original support scheme. In a soft rock roadway support, BF-CRM can effectively control the displacement and deformation of the floor, reducing the stress concentration in the surrounding rock and reducing the range over which the plastic zone extends.

Data Availability

The data used to support the findings of this study are included within the article.

Conflicts of Interest

The authors declare that they have no conflicts of interest.

Acknowledgments

This work was funded by the National Natural Science Foundation of China, China (Grant nos. 51774192 and 51474135), and the Postgraduate Technology Innovation Project of Shandong University of Science and Technology (Grant no. SDKDYC190239). This support is greatly appreciated.

References

- [1] L.-J. Hunag, H.-Y. Wang, and S.-Y. Wang, "A study of the durability of recycled green building materials in lightweight aggregate concrete," *Construction and Building Materials*, vol. 96, pp. 353–359, 2015.
- [2] Y. Yu and H. Zhu, "Influence of rubber size on properties of crumb rubber mortars," *Materials*, vol. 9, no. 7, p. 527, 2016.
- [3] Y. Yong, *Mechanism Study on the Influence of Rubber on Mortar Properties*, Tianjin University, Tianjin, China, 2016.
- [4] K. Bisht and P. V. Ramana, "Evaluation of mechanical and durability properties of crumb rubber concrete," *Construction and Building Materials*, vol. 155, pp. 811–817, 2017.
- [5] R. X. Hao, S. F. Dong, and X. Y. Guo, "The research of scrap tire rubber powder effect on the performance of cracking mortar," *Advanced Materials Research*, vol. 472–475, pp. 1777–1781, 2012.
- [6] Y. X. Yang and Q. R. Yue, "Application and study of basaltic fiber reinforced polymer," *Industrial Construction*, vol. 37, no. 6, pp. 1–4, 2007.
- [7] J. Sim, C. Park, and D. Y. Moon, "Characteristics of basalt fibre as a strengthening material for concrete structures," *Composites Part B: Engineering*, vol. 36, no. 6–7, pp. 504–512, 2005.
- [8] C. Colombo, L. Vergani, and M. Burman, "Static and fatigue characterisation of new basalt fibre reinforced composites," *Composite Structures*, vol. 94, no. 3, pp. 1165–1174, 2012.
- [9] V. Fiore, T. Scalici, G. Di Bella, and A. Valenza, "A review on basalt fibre and its composites," *Composites Part B: Engineering*, vol. 74, pp. 74–94, 2015.
- [10] H. D. Yan, X. F. Chen, X. X. Ma et al., "Experimental study of the properties of cement mortar with EPDM rubber powder admixture," *China Civil Engineering Journal*, vol. 41, no. 12, pp. 55–66, 2008.
- [11] G. C. Long, N. Li, Y. H. Xue et al., "Mechanical properties of self-compacting concrete incorporating rubber particles under impact load," *Journal of the Chinese Ceramic Society*, vol. 44, no. 8, pp. 1081–1090, 2016.
- [12] H. B. Zhang, X. M. Guan, M. F. Gou et al., "Investigation on the influence of rubber particle size on the compressive strength of cement mortar and concrete," *Bulletin of the Chinese Ceramic Society*, vol. 31, no. 4, pp. 931–934, 2012.
- [13] A. E. Richardson, K. A. Coventry, and G. Ward, "Freeze/thaw protection of concrete with optimum rubber crumb content," *Journal of Cleaner Production*, vol. 23, no. 1, pp. 96–103, 2012.
- [14] M. Hora and P. Reiterman, "Assessment of the air-entraining effect of the rubber powder and its influence on the frost resistance of concrete," *Revista Romana De Materiale-Romanian Journal of Materials*, vol. 46, no. 3, pp. 327–333, 2016.

- [15] S. Di, C. Jia, W. Qiao, K. Li, and K. Tong, "Energy evolution behavior and mesodamage mechanism of crumb rubber concrete," *Advances in Materials Science and Engineering*, vol. 2018, Article ID 9843416, 13 pages, 2018.
- [16] W. M. Li and J. Y. Xu, "Strengthening and toughening basalt fiber-reinforced concrete," *Journal of the Chinese Ceramic Society*, vol. 36, no. 4, pp. 476–486, 2008.
- [17] Y. Barabanshchikov and I. Gutskalov, "Strength and deformability of fiber reinforced cement paste on the basis of basalt fiber," *Advances in Civil Engineering*, vol. 2016, Article ID 6562526, 5 pages, 2016.
- [18] L. Fenu, D. Forni, and E. Cadoni, "Dynamic behaviour of cement mortars reinforced with glass and basalt fibres," *Composites Part B: Engineering*, vol. 92, pp. 142–150, 2016.
- [19] Y. Wang, J. Chen, D. Gao, and E. Huang, "Mechanical properties of steel fibers and nanosilica modified crumb rubber concrete," *Advances in Civil Engineering*, vol. 2018, Article ID 6715813, 10 pages, 2018.
- [20] M. L. Santarelli, F. Sbardella, M. Zuena, J. Tirillò, and F. Sarasini, "Basalt fiber reinforced natural hydraulic lime mortars: a potential bio-based material for restoration," *Materials & Design*, vol. 63, pp. 398–406, 2014.
- [21] W.-J. Song, W.-G. Qiao, X.-X. Yang, D.-G. Lin, and Y.-Z. Li, "Mechanical properties and constitutive equations of crumb rubber mortars," *Construction and Building Materials*, vol. 172, pp. 660–669, 2018.
- [22] Q. B. Meng, L. J. Han, F. G. Zhang, J. Zhang, J.-W. Nie, and S.-Y. Wen, "Coupling support effect on high-stress deep soft rock roadway and its application," *Rock and Soil Mechanics*, vol. 38, no. 5, pp. 1424–1435, 2017.
- [23] Q. B. Meng, L. J. Han, W. G. Qiao et al., "Numerical simulation research of bolt-grouting supporting mechanism in deep soft rock roadway," *Journal of Mining & Safety Engineering*, vol. 33, no. 1, pp. 27–34, 2016.
- [24] L. Wang, Y. Lu, Y. Huang, and H. Sun, "Deep-shallow coupled bolt-grouting support technology for soft rock roadway in deep mine," *Journal of China University of Mining & Technology*, vol. 45, no. 1, pp. 11–18, 2016.
- [25] Z. H. Guo, X. Q. Zhang, D. C. Zhang et al., "Experimental study on stress-strain curves of concrete," *Journal of Building Structures*, vol. 3, no. 1, pp. 3–14, 1982.

